A Bioelectronic Platform Using a Graphene–Lipid Bilayer Interface

Priscilla Kailian Ang,[†,‡,▽] Manu Jaiswal,[†,▽] Candy Haley Yi Xuan Lim,[†,‡] Yu Wang,[†] Jagadish Sankaran,[†] Ang Li,[§] Chwee Teck Lim,[⊥,¶] Thorsten Wohland,[†] Özyilmaz Barbaros,[#] and Kian Ping Loh[†,*]

[†]Department of Chemistry, National University of Singapore, 3 Science Drive 3, Singapore 117543, [‡]NUS Graduate School for Integrative Sciences and Engineering, Singapore 117597, [§]Singapore-MIT Alliance for Research & Technology (SMART), 28 Medical Drive, #05-06M, Singapore 117456, [⊥]Department of Mechanical Engineering and Division of Bioengineering, National University of Singapore, Singapore 117576, [¶]Mechanobiology Institute, National University of Singapore, Singapore 117411, and [#]Department of Physics, National University of Singapore, Singapore 117542. [▽]These authors contributed equally to this work.

ABSTRACT The electronic properties of graphene can be modulated by charged lipid bilayer adsorbing on the surface. Biorecognition events which lead to changes in membrane integrity can be monitored electrically using an electrolyte-gated biomimetic membrane–graphene transistor. Here, we demonstrate that the bactericidal activity of antimicrobial peptides can be sensed electrically by graphene based on a complex interplay of biomolecular doping and ionic screening effect.

KEYWORDS: graphene · lipid bilayer · membrane disruption · bioelectronic interface · biomolecular doping · ionic screening

Graphene is emerging as a new bioelectronic platform for sensing biomolecules owing to its chemical robustness and sensitivity to changes in its electromagnetic environment.[1−5] A graphene-based biosensor can potentially offer low noise and ultrasensitive electrical detection.[6] In line with a carbon microelectrode array that has been used for extracellular recording, it is interesting to evaluate the use of graphene for sensing action potential or membrane movement in cells. Regardless of the types of cells investigated, the cell membrane is inevitably the biological component that is in direct contact with graphene.[7] These cell membranes are frequently charged; its presence on graphene creates charged impurities which exert spatially inhomogeneous Coulomb potential, leading to finite minimum conductivity and doping of graphene.[8] The electronic properties of atomically thin graphene have been shown to be highly sensitive to changes in Coulomb potential exerted by charged inorganic impurities and also to screening effects arising from the dielectric environment.[9−12]

To evaluate the electrical response of graphene to charged lipid membranes, biomimetic membranes of different surface charges were assembled on graphene to form an active channel in an electrolyte-gated graphene field-effect transistor (FET). Biomimetic membranes are important *in vitro* mimics of cellular membranes.[13] The electric charge, thickness, and permeability of biomimetic membranes mimic the response of cells toward environmental factors and pathogenic agents. Herein, we demonstrate a proof-of-concept in which perturbation of the gram-negative bacteria biomimetic membrane by antimicrobial peptide, Magainin 2, results in changes to membrane properties which can be electrically detected by graphene.

RESULTS AND DISCUSSION

Characterization of Graphene Transistor. Figure 1a illustrates the design of our biomimetic membrane–graphene field-effect transistor. Chemical vapor deposited (CVD) graphene film is used as the electrical transduction platform because its large area, high electrical conductivity, and optical transparency afford the possibility of fabricating a dual-mode optical and electrical detection system. Raman spectroscopy was used to verify the quality and layer thickness of the CVD graphene film (Figure 1b). The negligible defect-related D band at around 1350 cm^{-1} indicates the high crystallinity of the CVD graphene film, while the ratio of the integrated intensity of G band (1586 cm^{-1}) to D′ band (2678 cm^{-1}) of 0.3[14] suggests the film to be a high quality monolayer. Figure 1c shows the water-gated ambipolar field-effect response of graphene. The drain/source contacts were insulated using silicon rubber and the gate leakage was less than 20 nA at the maximum applied voltage. The gate potential (V_g) is converted to units of charge carrier density n, (Figure 1d) using capacitance–voltage

*Address correspondence to chmlohkp@nus.edu.sg.

Received for review September 2, 2010 and accepted November 02, 2010.

Published online November 10, 2010.
10.1021/nn1022582

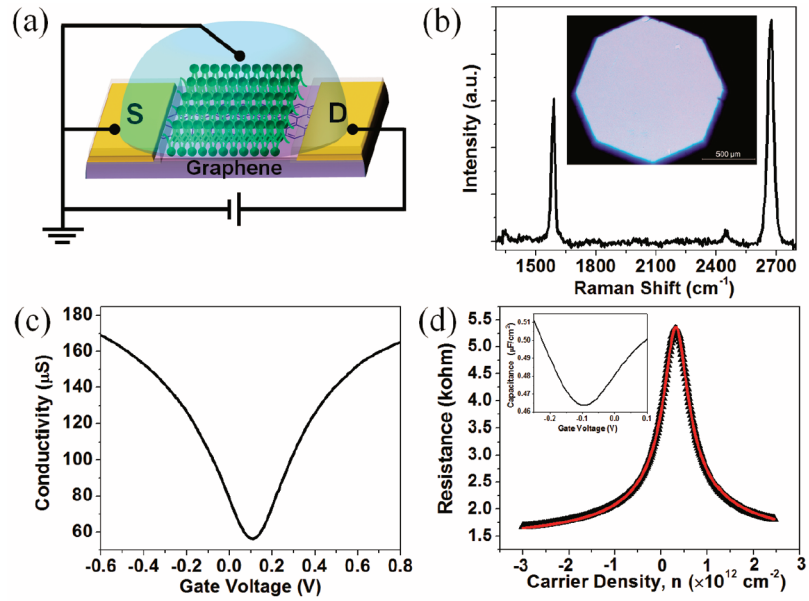

Figure 1. (a) Schematic representation of biomimetic membrane−graphene field effect transistor; (b) Raman spectrum of single layer CVD graphene. Inset shows optical image of CVD graphene film; (c) water-gated ambipolar FET response of device at V_{ds} = 100 mV; (d) resistance as a function of carrier density, *n*, where *n* is obtained by integrating over capacitance−voltage curve (inset). The red fitted curve allows the extraction of field-effect mobility and contact resistance.

(*C*−*V*) measurements. The charge carrier density is obtained by integrating the *C*−*V* curve

$$n(V_g - V_{g,min}) = \frac{1}{e}\int_{V_{g,min}}^{V_g} C(V)\, dV \qquad (1)$$

where *e* is the electronic charge, *C*(*V*) is the voltage-dependent total capacitance at the interface of graphene and $V_{g,min}$ is the potential at the charge neutrality point of graphene. The total capacitance of the graphene−electrolyte interface consists of a serial combination of solution double-layer capacitance C_i and quantum capacitance of graphene C_Q and was experimentally determined as a function of gate voltage (see inset in Figure 1d). The corresponding resistance−carrier density profiles can be fitted to the equation

$$R(n) = R_c + \frac{L}{We\mu_{FE}\sqrt{n_o^2 + (n - \bar{n})^2}} \qquad (2)$$

where *n* is the modulated carrier concentration, n_o is the residual carrier density, $\bar{n}$ is the shift in minimum conductivity, *L* and *W* are the length and width of the graphene device, respectively. This fitting equation allows the extraction of the field-effect mobility (μ_{FE}) and contact resistance (R_c). The shift in conductivity minimum is obtained by equating, R_1 (V_g = 0) = R_2 (*n* = 0) in the converted curves. The estimated charge carrier mobility is 2100 cm^2/(V s); however, a small asymmetry in hole and electron mobility is also noted from the fitted curve.

Quality of Biomimetic Membranes on Graphene. Owing to the high optical transparency of CVD graphene,[15,16] the spatial uniformity and dynamic fluidity of biomimetic membranes on graphene can be investigated by fluorescence techniques like imaging total internal reflection fluorescence correlation spectroscopy (ITIR-FCS) which provides high temporal resolution imaging of diffusion coefficient (lateral mobility) of lipids.[17,18] Biomimetic membranes constructed from 1-palmitoyl-2-oleoyl-*sn*-glycero-3-phosphocholine (POPC) lipids were assembled on graphene and glass *via* vesicle fusion. The diffusion coefficients, *D*, for the biomimetic membranes can be extracted from the theoretical fits of the autocorrelation function curves (ACFs) given by eq 1 in the Supporting Information, S1. The comparison between diffusion coefficients of neutral POPC membranes on graphene (1.85 ± 0.74 μm^2/s) and glass (2.66 ± 1.23 μm^2/s) shows that lipid mobilities of membranes on graphene are close to those obtained on glass (Figure 2a,b), which is surprising in view of the hydrophobic character of graphene.[19] The spatial uniformity of membranes atop glass and graphene is evident in Figure 2c,d in which the spatially resolved diffusion coefficient images show relatively constant membrane diffusivity. The corresponding average intensity images of the lipid membranes on glass and graphene are shown in Figure 2e,f, whereby the lipid membrane is uniform, homogeneous, and free from lipid aggregates. The good lateral mobility of biomimetic membranes on graphene suggests that a trapped water layer of reasonable thickness may exist between the graphene and biomimetic membrane.[20]

Influence of Charged Lipids on Graphene. The effects of charged lipid membranes on the Dirac point, charge carrier density, and mobilities of graphene FET are evaluated. Figure 3 panels a and b show the respective water-gated current−voltage (*I*−*V*) and

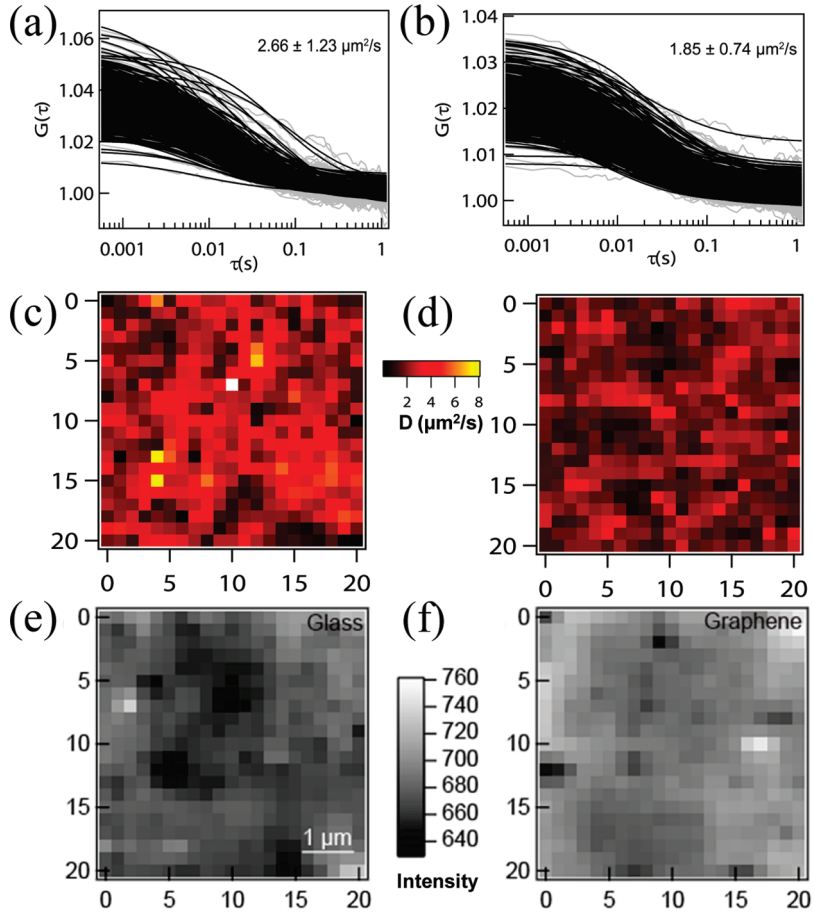

Figure 2. Autocorrelation function curves (ACFs) captured by ITIR-FCS for Rho-PE-labeled POPC bilayers. (a) ACFs of membranes on glass. (b) ACFs of membranes on graphene. The figures show all 441 correlation curves captured in a 21 pixel × 21 pixel region of interest on the EMCCD camera. The labeling ratio of Rho-PE/POPC was 0.01% for glass and 0.02% for graphene; the sample was excited with 2 mW at a wavelength of 514 nm; the recording time was 5.6 s for 10000 frames. The diffusion coefficient images (with the corresponding color scale) which confer spatial uniformity are shown for (c) glass and (d) graphene. The average fluorescent intensity image of membranes prepared on glass and graphene are presented in panels e and f, respectively.

capacitance−voltage ($C-V$) response of graphene while Figure 3c shows the derived resistance−carrier density plots when negatively charged (lipid composition 1-palmitoyl-2-oleoyl-*sn*-glycero-3-phosphocholine (POPC)/1-palmitoyl-2-oleoyl-*sn*-glycero-3-[phospho-rac-(1-glycerol)] (POPG) (2/1)), positively charged (lipid composition 1,2-dioleoyl-sn-glycero-3-phosphocholine (DOPC)/1,2-dioleoyl-3- trimethylammonium-propane (DOTAP) (2/1)) and neutral POPC membranes were subsequently assembled on the same graphene device after repetitive washing with 10% sodium dodecyl sulfate (SDS). Several key findings are summarized in Table 1. First, a small shift in Dirac point ($\Delta V_{g,min} = +0.12$ V) which corresponds to a change in carrier density of $\Delta n_{g,min} \approx 0.42 \times 10^{12}$ cm^{-2} is observed for the neutral lipids which is comparable to that of bare graphene in water. This shift could be attributed to the presence of negatively charged impurities trapped on the surface of SiO_2/Si substrate. The presence of neutral lipids, however, does not contribute to any additional shift in Dirac point. Second, it is noticed that the magnitude of Dirac point shift in the presence of negatively charged lipids ($\Delta V_{g,min} = +0.28$ V with respect to $V_g = 0$ V) is larger than that by positively charged lipids ($\Delta V_{g,min} = -0.1$ V with respect to $V_g = 0$ V), for the same magnitude of net lipid-charge. A possible reason is that positively charged lipids atop graphene induced a partial nullification of impurity potential generated by the underlying negatively charged surface impurities on SiO_2/Si substrate. Nevertheless, the magnitude of voltage shift from both positive and negative lipids is quite comparable, when this shift is measured from the position of conductivity minimum of bare graphene. The observed shifts of the Dirac point according to the sign of lipid charges is a consequence of charge-impurity potential generated by the lipid membranes and unequivocally demonstrate that the charged lipid membranes modulate the electronic properties of graphene significantly. Assuming an equal partitioning of charged lipids in the two leaflets since graphene is an electrically neutral substrate, the density of charged impurities in the lipid membranes can be estimated from the surface area associated with a lipid headgroup.[7,21,22] By assigning an area of 68 Å^2 to each lipid headgroup and noting that

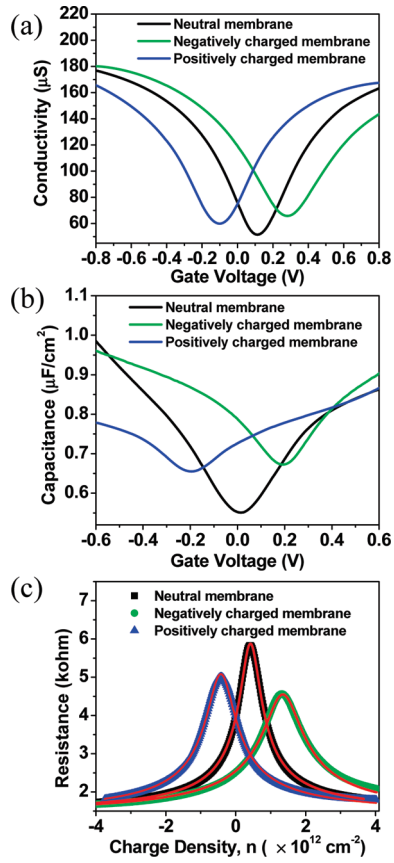

Figure 3. Electrical characterization and simulation of graphene coated with charged and neutral lipid membranes. (a) Current−voltage measurements of graphene coated with negatively charged (POPC/POPG = 2/1), positively charged (DOPC/DOTAP = 2/1), and neutral POPC membranes. (b) Capacitance−voltage measurements of different charged and neutral membranes on graphene in water. (c) Corresponding graphs of resistance *versus* carrier density. The red fitted curves allow the extraction of parameters shown in Table 1.

only 33% of the surface groups are charged, the estimated value of this impurity density is $n_{imp} \approx 5 \times 10^{13}$ cm^{-2}.[23] Unlike the immobile charges on SiO_2 surface, the lipids can diffuse along the surface of the membrane. Correlations between charged impurity scatterers are known to reduce the *effective* impurity density in semiconducting systems.[24] In addition, a complete large-area surface coverage of lipid membranes on substrates may not always be realized experimentally.[25−27] In view of these two considerations, a lower value was assigned to the impurity density arising from the charged membranes than that obtained from the headgroup surface area, $n_{imp} \approx 2.5 \times 10^{13}$ cm^{-2}. It is worth noting that typical values of charged impurities arising from the SiO_2 substrate range from 0.5×10^{12} to 5×10^{12} cm^{-2}.[9]

Next, we examine the influence of the charged lipids on the graphene charge carrier mobility. Experimentally, the charge carrier mobility shows a decrease upon formation of a negatively charged lipid membrane as compared to a neutral lipid membrane atop graphene (refer to Table 1; μ decreases by ∼25% after formation of a negatively charged lipid layer on graphene. The compared values are measured for the same sample). The mobility of graphene is given by $\mu = \sigma/ne$, in which the conductivity σ can be approximated within the Boltzmann regime as $\sigma = (e^2/h)(2E_F\tau/\hbar)$, where τ is the total scattering time and E_F is the chemical potential.[28] There are several possible sources of scattering and the total scattering rate τ^{-1} can be expressed as $1/\tau = 1/\tau_{SiOx} + 1/\tau_{SR} + 1/\tau_{CIL}$ where τ_{SiOx}, τ_{SR}, and τ_{CIL} represent the scattering time related to substrate charged impurities, short-range scatterers (such as defects), and lipid charged impurity, respectively. The former two scattering time scales represent the mobility-limiting factors *prior* to introduction of the lipid membrane, and a quantitative estimate of these two individual contributions *is not* central to the present work. The decrease in graphene mobility upon introduction of charged lipids is caused by the presence of additional scattering (τ_{CIL}), within the framework of a standard scattering problem for a screened Coulomb potential. One important consideration is that the effective interfacial dielectric function, ε, is also critically dependent on the thickness of the trapped water layer between the lipid membrane and graphene, *d*.[12] This separation, *d*, corresponds to the distance of lipid headgroup charges from the graphene plane. The presence of a water dielectric layer weakens the coupling between graphene and the impurity charges. In the case of a thick layer of trapped water, the effective dielectric constant can be estimated by averaging between that of the silicon oxide substrate and bulk water, $\varepsilon(d = \infty) \approx (\kappa_{SiO_2} + \kappa_{water})/2 \approx 41$. In the absence of trapped water layer ($d \rightarrow 0$), the relevant dielectric constant in this limit is $\varepsilon(d = \infty) \approx (\kappa_{SiO_2} + \kappa_{lipids})/2 \approx 3.3$, where the lipid dielectric constant (∼2.7) comes into play.[29] By comparing the experimentally observed change in mobility with the theoretically estimated influence of scattering from

TABLE 1. The Effect of Lipid Charges on Graphene Surface Potential, Charge Carrier Density, and Charge Carrier Mobility (Where Hole and Electron Mobility Are Nearly Identical)[a]

charged membranes	$\Delta V_{g,min}$ (volts)	$\Delta n_{g,min}$ ($\times 10^{12}$/cm^2)	n_0 ($\times 10^{12}$/cm^2)	μ_{FE} (cm^2/(V s))
POPC (neutral)	+0.12	+0.42	0.29	1608
POPC/POPG (2:1) (negative)	+0.28	+1.35	0.54	1200
DOPC/DOTAP (2:1) (positive)	−0.10	−0.42	0.40	1401

[a] $\Delta V_{g,min}$ corresponds to the Dirac point shift with respect to $V_g = 0$ V; $\Delta n_{g,min}$ represents the change in charged carrier density for the corresponding change in Dirac point position; n_0 is the residual carrier density obtained from the width of voltage plateau; μ_{FE} is the field-effect mobility.

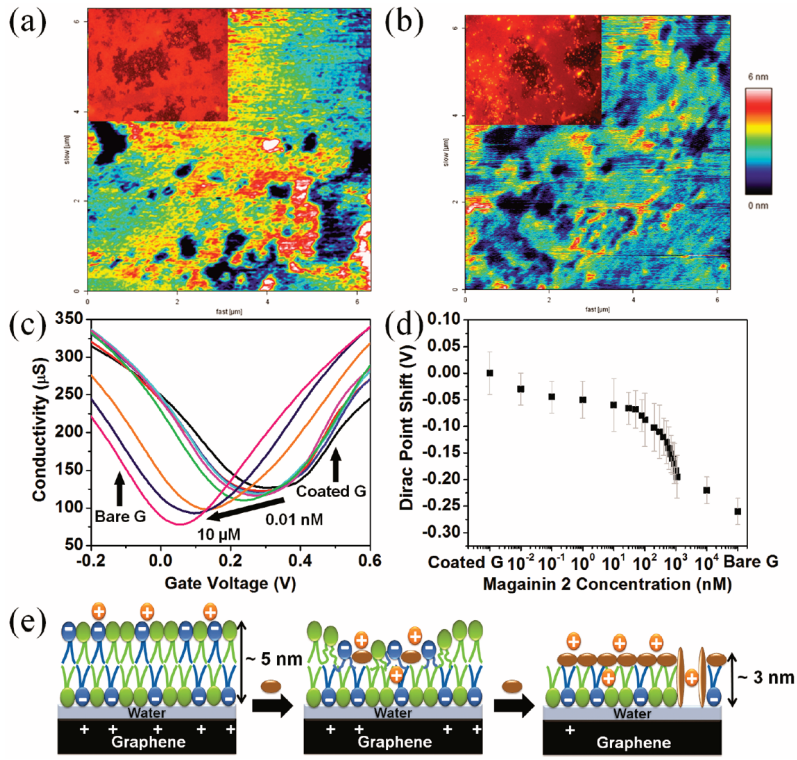

Figure 4. Membrane thinning effect of Magainin 2 peptides on gram-negative bacteria biomimetic membrane. AFM and epi-fluorescence (inset) images of membrane (a) before and (b) after addition of 1 μM Magainin 2 peptides. Peptide-induced membrane thinning was evident especially at the edge of lipid membrane patches. Inset shows the epi-fluorescence image in which adsorption of peptides (represented by bright spots) was clearly observed at the periphery of the membranes. These bright spots are speculated to be due to the onset of membrane thinning in which adsorbed peptides push apart the lipid headgroups on the top leaflet, causing these fluorescent lipids to be dislodged from the surface. (c) Conductivity curves of biomimetic membrane−graphene FET in 10 mM NaF with increasing Magainin 2 concentration and (d) the corresponding shifts in Dirac points. (e) Schematic diagram showing sensing concept of membrane thinning effect. Brown ovals represent peptides.

the density of lipid impurity charges $n_{imp} = 2.5 \times 10^{13}$ cm^{-2}, the value of impurity separation obtained is $d \approx 2.0 \pm 0.5$ nm. The value of effective dielectric constant at this separation is $\varepsilon \approx 26$, intermediate to the values for bulk water and lipid-membrane. It may be noted that about $d \approx 4$ nm of water is needed before the graphene interface is completely decoupled from the influence of the lipid dielectric environment (see Supporting Information, Figure S2). While the above estimates for impurity separation and effective dielectric constant represent a good approximation, the actual values for these may vary with the precise impurity concentration. The presence of this interfacial hydrated layer partially attenuates the Coulomb potential from the impurity charges, thus it is observed that the voltage-widths (arising from residual carriers) are not broadened and mobility for transfer curves is not degraded significantly, despite a higher density of impurity charges on the lipid membrane. These concepts can be further generalized to understand the influence of cellular media on the electronic properties of graphene, since the presence of a trapped water layer and an impurity-separation dependent dielectric-constant are central to both biophysical problems.

Electrical Detection of Membrane Disruption. The perturbation of gram-negative bacteria biomimetic membrane atop graphene FET can be induced by the antimicrobial peptide, Magainin 2, which is a 23-residue cationic peptide (NH_2-Gly-Ile-Gly-Lys-Phe-Leu-His-Ser-Ala-Lys-Lys-Phe-Gly-Lys-Ala-Phe-Val-Gly-Glu-Ile-Met-Asn-Ser-$CONH_2$) extracted from the skin of the African frog *Xenopus laevis*.[30,31] It adopts a primarily α-helical structure upon binding to negatively charged membrane by electrostatic attraction. Magainin 2 has two binding states in a membrane: (1) a surface state at low peptide concentration in which it adsorbs parallel to the membrane surface and (2) a transmembrane pore-forming state at high peptide concentration.[32,33] While the mechanism of peptide-induced membrane perforation has been a subject of much debate, there is increasing experimental evidence of membrane thinning as a precursor stage to pore formation.[32,34−39] Here, the membrane thinning effect can be clearly observed from the AFM and epi-fluorescence images when 1 μM Magainin 2 was added to the negatively charged POPC/POPG membranes (Figure 4a,b). A decrease in membrane thickness from ~5 ± 1 nm (Figure 4a) to ~3 ± 1 nm (Figure 4b) was detected.

The changes in membrane electric charge, thickness, and permeability induced by increasing concentration of Magainin 2 can be detected electrically. Figure 4c shows the conductivity curves for bare and biomimetic membrane-coated graphene gated with 10 mM NaF. Negatively charged membrane displays an increase in conductivity minimum value and a positive shift in Dirac point relative to that of bare graphene. This is due to an increase in residual impurity charges induced by the negatively charged membrane, as has been discussed earlier. Upon peptide addition, conductivity minimum value decreases and Dirac point shifts gradually toward that for bare graphene. The value of hole density can be estimated to decrease from $1.35 \times 10^{12}/cm^2$ (biomimetic membrane-coated graphene) to $0.82 \times 10^{12}/cm^2$ (upon addition of 1 μM Magainin 2). A sigmoidal Dirac point shift dependence on peptide-concentration plotted on a logarithmic concentration scale (Figure 4d) signifies cooperative effects in the peptide−membrane interaction and is a fingerprint for the transition from surface-bound state to pore-forming state.[32] A detection limit of 0.1 nM can be attained based on a detectable Dirac point shift of ~50 mV. This detection limit is consistent with the peptide-to-lipid molar ratio (P/L ≈ 1/150) for the onset of membrane thinning measured by X-ray diffraction[37] and oriented circular dichroism.[32] A control experiment where 1 μM cationic Magainin 2 peptides were added to bare graphene produced a much smaller shift in the Dirac point ($\Delta V_{g,min} \approx -0.03$ V) (Supporting Information, Figure S3) compared to that observed by peptide-induced perturbation of membrane electric charges ($\Delta V_{g,min} \approx -0.18$ V). This indicates a remarkably insignificant contribution of Coulomb potential arising from nonspecific binding of Magainin 2 peptides as compared to lipid charges on graphene.

Biosensing Mechanism. A schematic model illustrating the sensing mechanism of the biomimetic membrane−graphene FET is shown in Figure 4e. The principle for the electrical detection of membrane thinning is underpinned by the ionic screening effect of the electrolyte which contains NaF ions in necessarily low ionic strength. The impurity potential on graphene exerted by negatively charged membranes can be screened by the ionic solution within the Debye distance. On the bulk solution side of the lipids, the screening effect is determined by the solution of the Poisson−Boltzmann equation, $\psi''(x) = \lambda_D^{-2} \sinh \psi(x)$, where $\psi(x) = e\phi/(k_BT)$ is the reduced electrostatic potential.[40] The screening effect due to the ionic strength of the NaF solution is related to the Debye length of the ionic solution. According to the Graham equation simplified for 1:1 electrolyte solution, the Debye length (λ_D) is given by

$$\lambda_D = \frac{0.304}{\sqrt{[NaF]}} nm \quad (3)$$

and yields a value of ~3 nm for 10 mM NaF solution. As illustrated by the model, the intact lipid bilayer with a thickness of ~5 nm passivates the graphene from the ions in the solution. The adsorption of ions on the lipid membrane screens the charges of the top membrane leaflet but not the bottom leaflet proximal to graphene. The extremely low ion permeability of the membrane prevents the build-up of screening charges in the thin layer of water between the proximal membrane leaflet and graphene. It is this proximal leaflet adjacent to graphene that exerts the charge impurity potential on graphene. Upon the thinning or disruption of the membrane induced by Magainin 2 peptides, ions permeate closer to the surface of graphene and provide ionic screening of the impurity potential from the proximal membrane leaflet. It therefore follows that the ionic screening of the impurity charges can be switched on or off depending on the thickness of the membrane, which changes in response to the hemolytic activity of the membrane-disrupting agent.

CONCLUSION

We have demonstrated the effect of charged lipid membranes and the interplay of charged impurity and ionic screening mechanism in the control of electrical response in a biomimetic membrane-coated graphene biosensor. Charged biomimetic membrane imposes an impurity potential which causes voltage shifts in the charge neutrality point and increases minimum conductivity. The impurity potential is screened by mobile ions upon thinning or disruption of the membrane by a membrane-disrupting agent, leading to a recovery of the voltage-shift initially induced by the uncoated graphene plane. The sensing concept developed here based on the dynamics of membrane diffusion and changes in ionic screening on graphene may be extended to other biorecognition systems such as ligand−receptor binding and gated control of ion channels embedded in membranes.

METHODS

Fabrication of CVD Graphene Film. CVD growth and transfer of the graphene film was based on methods developed by Ruoff *et al.*[15] and Hong *et al.*[16] A monolayer of chemical-vapor-deposited (CVD) graphene was grown on a piece of 0.025 mm thick Cu foil (Alfa Aesar, 99.8%). The Cu foil was inserted into a quartz tubular reactor and heated to 1000 °C in 10 sccm of flowing H_2 at 1.01 Torr. After 1000 °C was attained, CH_4 was injected into the reactor at 110 sccm for 30 min before the system was cooled to room temperature in 10 sscm of H_2. After the growth process, 100 μL of 3% polymethylmethacrylate (PMMA) (molecular mass, 950K) chlorobenzene solution was spin-coated onto the Cu foil at 4000 rpm using a spincoater (Spin150, APT GmbH). The thickness of PMMA was about 300 nm. The Cu foil was etched in 0.5 M $FeCl_3$. After etching, the graphene films were rinsed copiously to remove the residual etchant, and then transferred onto cover

glass for fluorescence study, or onto SiO_2/Si substrates with oxide thickness of 285 nm for field-effect measurements. The CVD graphene film was transferred onto the desired substrate and the PMMA film was dissolved in acetone at 50 °C for 12 h and the substrate was cleaned with isopropyl alcohol. The resultant CVD graphene on the desired substrate was then annealed in an atmosphere of Ar/H_2 gas (50/50 sccm) at 350 °C for 3 h in a tube furnace to remove residual PMMA.

Fabrication and Measurement of CVD Graphene Field Effect Transistor (FET). High quality silver paste (SPI supplies) was used as source of drain electrodes at the two ends of the graphene film (approximately 5 mm × 3 mm). Chemically inert silicon rubber was used to prevent direct contact between any metal and the electrolyte, leaving the active graphene area defined by the silicone rubber well (1 mm × 3 mm) exposed to the electrolyte solution (either water or 10 mM NaF). The electrical performance of the CVD graphene FETs was determined by measuring the standard two-probe configuration of top-gated device's static characteristics (drain−source current (IDS) *versus* gate voltage (VG) at constant drain−source voltage (VDS) of 100 mV). These characteristics were measured using the Keithley 4200 Semiconductor Characterization System with an Ag/AgCl gate electrode. Although two-probe configuration introduces contact resistance, the discussion on the relative changes in graphene charge carrier density and mobilities induced by different lipid charges remains valid.

Formation of Biomimetic Membranes on Graphene. Palmitoyl-2-oleoyl-*sn*-glycero-3-phosphocholine (POPC), 1-palmitoyl-2-oleoyl-*sn*-glycero-3-[phospho-rac-(1-glycerol)] (popg), 1,2-dioleoyl-*sn*-glycero-3-phosphocholine (dopc), 1,2-dioleoyl-3-trimethylammonium-propane (DOTAP), and 1,2-dipalmitoyl-*sn*-glycerol-3-phosphoethanolamine-*N*-(lissamine rhodamine B sulfonyl) ammonium salt (Rho-PE) were obtained from Avanti Polar Lipids (Alabaster, AL). POPC, prepared as stock in $CHCl_3$, was mixed with Rho-PE (concentration of 0.01% for glass and 0.02% for graphene) and then subjected to vacuum evaporation for 1 h. Rho-PE was added to the POPC lipid mixture for fluorescence study while unlabeled lipids: POPG, DOPC, and DOTAP were used for FET measurements. The evaporation was carried out in clean round-bottomed flasks. Prior to lipid addition, the flasks were cleaned in Piranha reagent (concentrated H_2O_2/H_2SO_4 = 3:1), washed with deionized (DI) water and technical ethanol, and dried before use. Phosphate buffer saline (PBS) was added to make 0.5 mM lipid suspension. A 2−6 mL portion of the suspension was sonicated for 30−45 min to form vesicles; 2 mL of the sonicated suspension was dispensed onto a petridish with cover glass bottom (World Precision Instruments, Inc., Sarosota, FL). In the case of graphene preparation, the graphene was fixed over the cover glass bottom in the chamber using silicone rubber. This was followed by incubation of sonicated vesicles on the substrates for 2−3 h at 60 °C for the formation of bilayers on glass or graphene. This was followed by cooling for 30 min. The lipid aggregates above the bilayer were washed by replacing the solution 10−20 times with PBS. It is crucial to soak the CVD graphene sample in distilled water (Nanopure) for a day prior to deposition of biomimetic membranes *via* vesicle fusion for better membrane formation. This is to prevent a widespread adsorption of unfused lipid vesicles rather than formation of a spatially uniform membrane. The lipid membrane must be wetted in buffer solution all the time to prevent disintegration.

ITIR-FCCS Instrumentation. Imaging total internal reflection-fluorescence correlation spectroscopy (ITIR-FCS) measurements were performed using an objective-type total internal reflection fluorescence microscope (TIRFM). This TIRFM is built using an inverted epifluorescence microscope (IX-71, Olympus) with a high NA oil-immersion objective (100×/NA1.45) (Olympus, Singapore). The fluorophores were excited with the 514 nm laser line of a dual color air-cooled Argon ion laser (185-F02, Spectra-Physics, Mountain View, CA). Imaging and spectroscopy were carried out using an electron multiplying charge-coupled device (EMCCD) camera (Andor iXON 860) mounted at the side-port of the microscope. The camera and microscope are controlled by the software Andor Solis (version 4.9.30000.0). The image capture region of 128 pixels × 128 pixels occupies 3.1 × 3.1 mm^2 on the chip. Hence each pixel measures 24 × 24 μm^2 on the chip and measures 240 × 240 nm^2 in the sample. The temporal resolution achieved is 0.56 ms for a region of interest of 21 pixels × 21 pixels.

Capacitance−Voltage Measurements. A three-electrode setup was used for capacitance−voltage measurements, consisting of an Ag/AgCl reference electrode and a Pt wire counter-electrode. The *C*−*V* graphs were recorded with Autolab PGSTAT30 digital potentiostat/galvanostat with FRA 4.9 software (Eco Chemie, The Netherlands). A small ac modulation of 100 Hz and voltage amplitude of 10 mV were applied over the potential range between −0.8 and +0.8 V. A small background capacitance of ~5 pF was obtained in the absence of graphene and can be attributed to connection electrodes, cables, and sample holder.

Atomic Force Microscopy (AFM) and Epifluorescence Measurements. Representative tapping mode AFM and epifluorescence images of lipid membranes were obtained using Nanowizard II BioAFM (JPK Instruments) incorporated with a confocal inverted microscope equipped with epifluorescence (Fluoview FV1000, IX81, Olympus). The fluorescence images were captured using a color CCD camera (JPK). The spring constants of the cantilevers were determined by the thermal tune method and were typically in the range of 0.3 ± 0.1 N/m. The AFM imaging was taken in PBS in a liquid sample holder and the peptides were injected through the perfusion inlet of the holder during scanning.

Acknowledgment. The authors are grateful for financial support by NRF-CRP grant "Graphene Related Materials and Devices" R-143-000-360- 281. T. Wohland gratefully acknowledges support by a grant from the Ministry of Education of Singapore, R-143-000-358-112.

Supporting Information Available: Principles of imaging total internal reflection fluorescence correlation spectroscopy (ITIR-FCS), simulated results of graphene conductivity *versus* carrier density and current−voltage measurement of bare graphene with Magainin 2. This material is available free of charge *via* the Internet at http://pubs.acs.org.

REFERENCES AND NOTES

1. Ang, P. K.; Chen, W.; Wee, A. T. S.; Loh, K. P. Solution-Gated Epitaxial Graphene as pH Sensor. *J. Am. Chem. Soc.* **2008**, *130*, 14392–14393.
2. Cohen-Karni, T.; Qing, Q.; Li, Q.; Fang, Y.; Lieber, C. M. Graphene and Nanowire Transistors for Cellular Interfaces and Electrical Recording. *Nano Lett.* **2010**, *10*, 1098–102.
3. Dong, X. C.; Shi, Y. M.; Huang, W.; Chen, P.; Li, L. J. Electrical Detection of DNA Hybridization with Single-Base Specificity Using Transistors Based on CVD-Grown Graphene Sheets. *Adv. Mater.* **2010**, *22*, 1649–1653.
4. Mohanty, N.; Berry, V. Graphene-Based Single-Bacterium Resolution Biodevice and DNA Transistor: Interfacing Graphene Derivatives with Nanoscale and Microscale Biocomponents. *Nano Lett.* **2008**, *8*, 4469–4476.
5. Ohno, Y.; Maehashi, K.; Yamashiro, Y.; Matsumoto, K. Electrolyte-Gated Graphene Field-Effect Transistors for Detecting pH Protein Adsorption. *Nano Lett.* **2009**, *9*, 3318–3322.
6. Yang, W.; Ratinac, K. R.; Ringer, S. P.; Thordarson, P.; Gooding, J. J.; Braet, F. Carbon Nanomaterials in Biosensors: Should You Use Nanotubes or Graphene. *Angew. Chem., Int. Ed.* **2010**, *49*, 2114–38.
7. Kataoka-Hamai, C.; Inoue, H.; Miyahara, Y. Detection of Supported Lipid Bilayers Using Their Electric Charge. *Langmuir* **2008**, *24*, 9916–9920.
8. Wehling, T. O.; Katsnelson, M. I.; Lichtenstein, A. I. Adsorbates on Graphene: Impurity States and Electron Scattering. *Chem. Phys. Lett.* **2009**, *476*, 125–134.
9. Adam, S.; Hwang, E. H.; Galitski, V. M.; Das Sarma, S. A Self-Consistent Theory for Graphene Transport. *Proc. Natl. Acad. Sci. U.S.A.* **2007**, *104*, 18392–18397.
10. Chen, F.; Xia, J. L.; Tao, N. J. Ionic Screening of Charged-Impurity Scattering in Graphene. *Nano Lett.* **2009**, *9*, 1621–1625.
11. Jang, C.; Adam, S.; Chen, J. H.; Williams, E. D.; Das Sarma, S.;

Fuhrer, M. S. Tuning The Effective Fine Structure Constant in Graphene: Opposing Effects of Dielectric Screening on Short- and Long-Range Potential Scattering. *Phys. Rev. Lett.* **2008**, *101*, 146805.
12. Ponomarenko, L. A.; Yang, R.; Mohiuddin, T. M.; Katsnelson, M. I.; Novoselov, K. S.; Morozov, S. V.; Zhukov, A. A.; Schedin, F.; Hill, E. W.; Geim, A. K. Effect of a High-Kappa Environment on Charge Carrier Mobility in Graphene. *Phys. Rev. Lett.* **2009**, *102*, 206603.
13. Loose, M.; Schwille, P. Biomimetic Membrane Systems To Study Cellular Organization. *J. Struct. Biol.* **2009**, *168*, 143–151.
14. Graf, D.; Molitor, F.; Ensslin, K.; Stampfer, C.; Jungen, A.; Hierold, C.; Wirtz, L. Spatially Resolved Raman Spectroscopy of Single- and Few-Layer Graphene. *Nano Lett.* **2007**, *7*, 238–242.
15. Li, X.; Zhu, Y.; Cai, W.; Borysiak, M.; Han, B.; Chen, D.; Piner, R. D.; Colombo, L.; Ruoff, R. S. Transfer of Large-Area Graphene Films for High-Performance Transparent Conductive Electrodes. *Nano Lett.* **2009**, *9*, 4359–4363.
16. Kim, K. S.; Zhao, Y.; Jang, H.; Lee, S. Y.; Kim, J. M.; Ahn, J. H.; Kim, P.; Choi, J. Y.; Hong, B. H. Large-Scale Pattern Growth of Graphene Films for Stretchable Transparent Electrodes. *Nature* **2009**, *457*, 706–710.
17. Sankaran, J.; Manna, M.; Guo, L.; Kraut, R.; Wohland, T. Diffusion, Transport, and Cell Membrane Organization Investigated by Imaging Fluorescence Cross-Correlation Spectroscopy. *Biophys. J.* **2009**, *97*, 2630–2639.
18. Kannan, B.; Guo, L.; Sudhaharan, T.; Ahmed, S.; Maruyama, I.; Wohland, T. Spatially Resolved Total Internal Reflection Fluorescence Correlation Microscopy Using an Electron Multiplying Charge-Coupled Device Camera. *Anal. Chem.* **2007**, *79*, 4463–4470.
19. Leenaerts, O.; Partoens, B.; Peeters, F. M. Water on Graphene: Hydrophobicity and Dipole Moment Using Density Functional Theory. *Phys. Rev. B* **2009**, *79*, 235440.
20. Hu, W.; Peng, C.; Luo, W.; Lv, M.; Li, X.; Li, D.; Huang, Q.; Fan, C. Graphene-Based Antibacterial Paper. *ACS Nano* **2010**, *4*, 4317–4323.
21. Robinson, A. J.; Richards, W. G.; Thomas, P. J.; Hann, M. M. Head Group and Chain Behavior in Biological-Membranes—A Molecular-Dynamics Computer-Simulation. *Biophys. J.* **1994**, *67*, 2345–2354.
22. Seelig, J.; Macdonald, P. M.; Scherer, P. G. Phospholipid Head Groups as Sensors of Electric Charge in Membranes. *Biochemistry* **1987**, *26*, 7535–7541.
23. Beschiaschvili, G.; Seelig, J. Melittin Binding To Mixed Phosphatidylglycerol Phosphatidylcholine Membranes. *Biochemistry* **1990**, *29*, 52–58.
24. Efros, A. L.; Pikus, F. G.; Burnett, V. G. Density of States of a 2-Dimensional Electron-Gas in a Long-Range Random Potential. *Phys. Rev. B* **1993**, *47*, 2233–2243.
25. Kim, Y. H.; Rahman, M. M.; Zhang, Z. L.; Misawa, N.; Tero, R.; Urisu, T. Supported Lipid Bilayer Formation by the Giant Vesicle Fusion Induced by Vesicle−Surface Electrostatic Attractive Interaction. *Chem. Phys. Lett.* **2006**, *420*, 569–573.
26. Richter, R. P.; Berat, R.; Brisson, A. R. Formation of Solid-Supported Lipid Bilayers: An Integrated View. *Langmuir* **2006**, *22*, 3497–505.
27. Rigby-Singleton, S. M.; Davies, M. C.; Harris, H.; O'Shea, P.; Allen, S. Visualizing the Solubilization of Supported Lipid Bilayers by an Amphiphilic Peptide. *Langmuir* **2006**, *22*, 6273–6279.
28. Nomura, K.; MacDonald, A. H. Quantum Hall Ferromagnetism in Graphene. *Phys. Rev. Lett.* **2006**, *96*, 256602.
29. Plant, A. L.; Gueguetchkeri, M.; Yap, W. Supported Phospholipid/Alkanethiol Biomimetic Membranes—Insulating Properties. *Biophys. J.* **1994**, *67*, 1126–1133.
30. Yang, L.; Weiss, T. M.; Lehrer, R. I.; Huang, H. W. Crystallization of Antimicrobial Pores in Membranes: Magainin and Protegrin. *Biophys. J.* **2000**, *79*, 2002–2009.
31. Zasloff, M.; Martin, B.; Chen, H. C. Antimicrobial Activity of Synthetic Magainin Peptides and Several Analogs. *Proc. Natl. Acad. Sci. U.S.A.* **1988**, *85*, 910–913.
32. Chen, F. Y.; Lee, M. T.; Huang, H. W. Evidence for Membrane Thinning Effect as the Mechanism for Peptide-Induced Pore Formation. *Biophys. J.* **2003**, *84*, 3751–3758.
33. Matsuzaki, K.; Sugishita, K.; Ishibe, N.; Ueha, M.; Nakata, S.; Miyajima, K.; Epand, R. M. Relationship of Membrane Curvature to the Formation of Pores by Magainin 2. *Biochemistry* **1998**, *37*, 11856–11863.
34. Heller, W. T.; Harroun, T. A.; Weiss, T. M.; Yang, L.; Waring, A. J.; Lehrer, R. I.; Huang, H. W. Membrane Thinning Induced by Protegrin-1: Clues to the Mode of Antibacterial Action. *Biophys. J.* **1999**, *76*, A215.
35. Heller, W. T.; Waring, A. J.; Lehrer, R. I.; Harroun, T. A.; Weiss, T. M.; Yang, L.; Huang, H. W. Membrane Thinning Effect of the Beta-Sheet Antimicrobial Protegrin. *Biochemistry* **2000**, *39*, 139–145.
36. Hung, W. C.; Chen, F. Y.; Lee, C. C.; Sun, Y.; Lee, M. T.; Huang, H. W. Membrane-Thinning Effect of Curcumin. *Biophys. J.* **2008**, *94*, 4331–4338.
37. Ludtke, S.; He, K.; Huang, H. Membrane Thinning Caused by Magainin 2. *Biochemistry* **1995**, *34*, 16764–16769.
38. Ludtke, S. J.; He, K.; Harroun, T.; Heller, W. T.; Huang, H. W. Lipid Dependence of Membrane Thinning Caused by Magainin, Melittin and Alamethicin. *Biophys. J.* **1996**, *70*, SU425.
39. Mecke, A.; Lee, D. K.; Ramamoorthy, A.; Orr, B. G.; Holl, M. M. B. Membrane Thinning Due to Antimicrobial Peptide Binding: An Atomic Force Microscopy Study of MSI-78 in Lipid Bilayers. *Biophys. J.* **2005**, *89*, 4043–4050.
40. Wagner, A. J.; May, S. Electrostatic Interactions across a Charged Lipid Bilayer. *Eur. Biophys. J. Biophy.* **2007**, *36*, 293–303.